

See discussions, stats, and author profiles for this publication at: <https://www.researchgate.net/publication/282410869>

Infrared thermography to study endwall cooling and heat transfer in turbine stator vane passages using the auxiliary wall method and comparison to numerical simulations

Article in *Quantitative InfraRed Thermography Journal* · September 2015

DOI: 10.1080/17686733.2015.1066135

CITATIONS

10

5 authors, including:



Holger Werschnik

SCHENCK RoTec, Darmstadt, Germany

10 PUBLICATIONS 189 CITATIONS

[SEE PROFILE](#)



Jonathan Hilgert

Technical University of Darmstadt

4 PUBLICATIONS 79 CITATIONS

[SEE PROFILE](#)

READS

51



Tom Ostrowski

Technical University of Darmstadt

6 PUBLICATIONS 29 CITATIONS

[SEE PROFILE](#)



Heinz-Peter Schiffer

Technical University of Darmstadt

162 PUBLICATIONS 2,202 CITATIONS

[SEE PROFILE](#)

Infrared thermography to study endwall cooling and heat transfer in turbine stator vane passages using the auxiliary wall method and comparison to numerical simulations

Holger Werschnik*, Tom Ostrowski, Jonathan Hilgert, Marius Schneider and Heinz-Peter Schiffer

Institute of Gas Turbines and Aerospace Propulsion, Technische Universität Darmstadt, Darmstadt, Germany

(Received 13 August 2014; accepted 17 June 2015)

Experiments using the auxiliary wall method and infrared thermography allow to study film cooling and heat transfer in turbomachinery research with high spatial resolution. Using heater foils and pulse width modulation, an aluminium body is heated to constant wall temperature, controlled by thermocouples. The heat flux is then determined across a low conductivity layer of Ethylene-Tetrafluoroethylene (ETFE), whereby 1-D conduction is assumed. Setting the base body to several quasi-steady state wall temperatures allows to deduce adiabatic wall temperatures and heat transfer coefficients. Given a coolant and main flow with different temperature, cooling effectiveness can be calculated, using a superposition approach. Experiments in the linear cascade test rig of the Institute for Gas Turbines and Aerospace Propulsion have been performed to study the effect of hub side coolant injection on the endwall heat transfer of a turbine stator row. The quality of results is examined through extensive data analysis, accompanied by a numerical simulation of the experiment.

Keywords: turbine endwall heat transfer; film cooling; experimental fluid dynamics; auxiliary wall method; infrared thermography

1. Endwall film-cooling, heat transfer and lean combustion

Modern gas turbines and jet engines aim to increase the turbine inlet temperature, which is a consequence of the continuous strive to increase the overall cycle efficiency with a higher compressor pressure ratio. Being far higher than acceptable material temperatures this means, that the endwall of the first stator row requires efficient cooling techniques and the flow needs to be well-understood in terms of convective heat transfer. To reduce the flow temperature in the vicinity of the endwall, coolant air is injected through holes upstream of the first stator row. This coolant air can also act as a protective layer.

Endwall film cooling in axial turbines has been studied experimentally by Friedrichs.[1] He states three main factors with influence on endwall heat transfer: The inlet temperature distribution, the thickness of the boundary layer and the three-dimensional flow field near the endwall. The latter is predominantly influenced by the secondary vortex system in a vane passage, which is also the crucial factor determining

*Corresponding author. Email: werschnik@glr.tu-darmstadt.de

the endwall heat transfer, according to Han et al. [2]. The model from Goldstein and Spores [3] illustrates this flow field (Figure 1) and mentions two dominating pressure gradients being responsible: The horseshoe vortex (Figure 1, No. 1. & 2.) is induced by the stagnation pressure gradient in the incoming boundary layer, which is converted into a static pressure gradient when approaching the leading edge of the vane. This forces the flow to turn towards the endwall and break up into two vortex structures. One leg is entering the passage along the suction side of the vane (Figure 1, No. 2.) and the other along the pressure side of the vane (Figure 1, No. 1.) with opposing rotational direction. The turning of the vanes induces the second important pressure gradient within the passage from the pressure side of the vane to the opposing suction side. A larger vortex structure starts to develop, denoted as the passage vortex (Figure 1, No. 3.), where the pressure side leg of the horseshoe vortex encounters the vane surface, at its shoulder, after travelling through the vane passage. The suction side leg of the horseshoe vortex remains close to the endwall up to a certain point, where it lifts off as well and starts to roll around the passage vortex with opposing rotational direction. Further low-momentum vortices develop at the airfoil corners (Figure 1, No. 4., 5. and 6.), denoted as corner vortices. Horseshoe and passage vortex cause the formation of a three-dimensional separation line for the inlet boundary layer. Downstream of the separation line, a highly skewed new boundary layer begins to develop, fed by downwash from the vane's pressure side (Figure 1, No. 8.). An attachment line divides fluid that enters one vane passage from the fluid entering the subsequent one. Where this line intersects the separation line, a saddle point is found. This vortex system is similar for all vane passages and determines heat transfer peak and minimum regions on the endwall. Friedrichs [1] gives an overview of existing experimental work and states the common understanding of high heat transfer regions as shown in Figure 2.

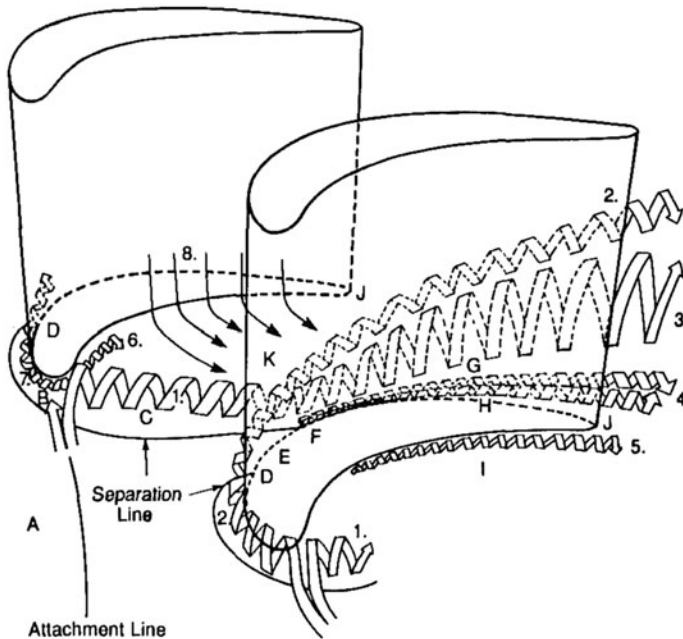


Figure 1. Vane passage vortex system from Goldstein and Spores [3].

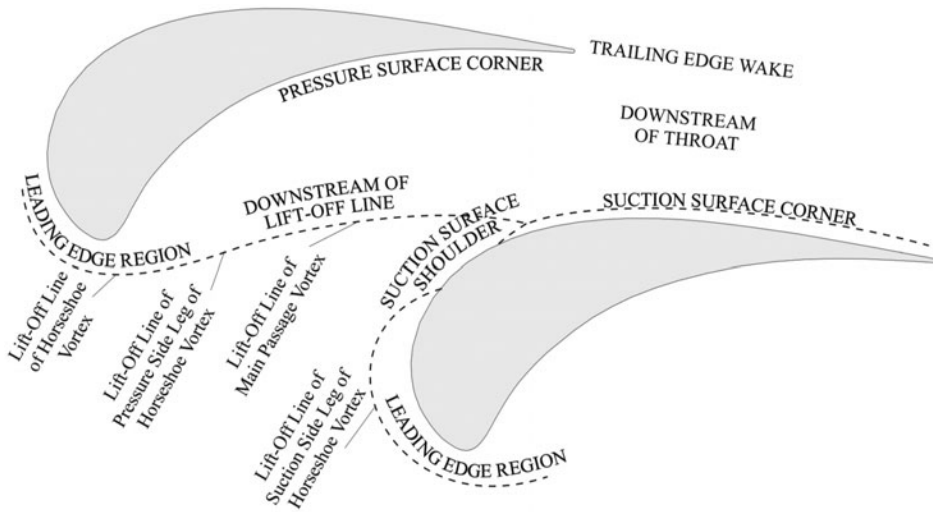


Figure 2. High endwall heat transfer regions according to Friedrichs [1].

According to Dückerhoff [4], a film cooling process is influenced by aerodynamic (density rate, blowing rate, turbulence level), geometric (hole geometry, angle and shape) and machine parameters (unsteady effects). Film cooling thereby has a large influence on the incoming endwall boundary layer, which can both be reenergized or weakened by the coolant injection and in this way influence the position of characteristic flow features and their effect on heat transfer. Aside from its effect on endwall heat transfer, film cooling also influences the aerodynamic losses in a stator passage: When injected upstream of the vortex lift-off line, the formation of the horseshoe-vortex and other secondary flow structures within the passage can be attenuated and their associated losses can be reduced according to Friedrichs [5] for certain blowing rates and injection geometries. Due to high losses within the injection holes themselves and mixing losses between coolant and main stream however, the overall losses are increased in any case. Coolant injection upstream of the separation line, as modelled in the present study can contribute in cooling a significant part of the endwall up to the separation line.

A driving factor for the research and work presented is the development of future aeroengine combustors which focuses on reducing pollutant emissions as well as increasing efficiency. Whereas a high turbine inlet temperature is in favour of the latter, this increases the NO_x -emissions as well. Demanded by legislative requirements, a reduction is necessary instead according to Lazik et al. [6]. This is hardly achievable with existing designs. The important factors of combustion temperature and reaction time have a major influence on the NO_x -level. The equivalence ratio has to be carefully selected: Whereas a low equivalence ratio has a positive influence on NO_x -emissions, it also has an adverse effect on flame stability and ignitability. To overcome this problem, a combustor concept known as lean combustion has been developed. Increased swirl in the combustion region is used to create a recirculation zone to stabilise a lean combustion.

From the point of view of turbine design, this however poses challenges: The increased combustor swirl is not fully attenuated until turbine inlet, and as a

consequence affects turbine performance as well as cooling. Moreover, the temperature distribution is changed: A more homogenous distribution is created and hence higher air temperatures near the stator endwall occur. Therefore, its cooling is a crucial factor for the development of the lean combustion concept and needs to be accompanied by experiments on realistic combustor geometries. This underlines the need for the measurement technique presented in this work, which is developed to yield this data on 3D-shaped surface geometries and in a rotating annular rig.

2. Endwall heat transfer measurement in turbomachinery – an overview

There are various experimental methods to quantify convective heat transfer for flow situations with and without coolant injection of which a brief overview will be given.

The local heat transfer on a surface is physically depending on the temperature gradient within the boundary layer of the near-wall flow. Due to its small scale, this gradient is hard to measure experimentally, which is shown by Han and Goldstein [7]. They used a butt-welded small-scale thermocouple on a traversable mount to study thermal boundary layer profiles near a turbine stator endwall. The technique is limited by conduction errors in thin boundary layers and challenging since the probe is hard to position when the flow velocity is high.

Due to similar limitations, most methods determine the local heat transfer with a coefficient HTC, which compares the local heat flux resulting from a temperature difference between the wall and a certain reference temperature (Equation (1)).

$$\text{HTC}(x,y) = \frac{\dot{q}(x,y)}{T(x,y) - T_{\text{ref}}} \quad (1)$$

Various heat transfer measurement techniques have been used to study vane endwall heat transfer with spatial resolution. Notable studies yielding surface heat transfer data for turbine endwalls include Blair [8], Goldstein and Spores [3], Graziani et al. [9] and Giel et al. [10,11], among others. Blair [8] conducted research on local film cooling effectiveness and heat transfer values in a linear cascade. Goldstein and Spores [3] used an indirect measurement method: The heat and mass transfer analogy with the naphthalene sublimation technique provides a way to acquire representative Stanton numbers for the whole endwall region between two turbine vanes. They discovered peak heat transfer regions and showed their correlation to the secondary vortex system in the passage. The importance of high resolution data for the interpretation of results was explained. Moreover, they further discovered evidence which helped in understanding the formation of the pressure side and suction side corner vortices. Airfoil and endwall heat transfer was also measured by Graziani et al. [9] in a linear cascade using a direct measurement technique with a constant-heat-flux-approach on the surfaces of interest: Surface Thermocouples were placed on strip heaters to gain a high spatial resolution in expected areas of high heat transfer gradients. The study also shows the effect of the inlet boundary layer thickness: For a thin boundary layer, the three-dimensional separation line moves further down into the passage. The streamlines downstream of the separation line are nearly perpendicular to the endwall pressure field, whereas the heat transfer contours exhibit an angle to it. A low heat transfer region is discovered near the pressure side. All methods are a challenge for experimental work, since both the heat flux and the driving temperature gradient have to be measured and because of the limited accessibility in test rigs. Giel et al. [10,11] studied heat transfer on turbine

blades and endwalls, using a constant wall temperature approach. They applied thermochromic liquid crystals on well-conductive material, which was covered by a low-conductive material, yielding local heat transfer values with high resolution with the advantage, that conduction problems into the structure can be avoided.

A detailed overview of other direct heat transfer measurement techniques can be found in Kaiser [12].

3. Experimental technique – the auxiliary wall method

The presented experimental method uses a near adiabatic auxiliary wall, which is made of an insulating material. It covers a metal base material which is known to have a high coefficient of heat conduction. Copper or aluminium can be considered technically useful materials, since there is usually enough manufacturing experience and availability of these materials in machining shops. For the present study, an aluminium AlMgSi1 alloy with a thermal conduction coefficient of more than 150 W/(mK) has been used. The base material is heated to a constant temperature level using heater foils (see Figure 3). Local differences in heat flux appear but are homogenised by the well conducting base material resulting in a near-uniform temperature distribution underneath the auxiliary wall. To define a local heat transfer coefficient, heat flux rates are calculated using the temperature gradient across the auxiliary wall (Equation (2)). Similar approaches to study turbomachinery heat transfer can be found in Giel et al. [10,11], Martini et al. [13] and Laveau et al. [14].

The auxiliary wall is manufactured from ethylene tetrafluoroethylene (ETFE). This material has been chosen due to its glass transition temperature being out of the target temperature range for the experiments and its low thermal conductivity. The method assumes that the local heat flux being transferred from the wall into the flow has to pass through the wall itself before and that no significant conductive heat transport occurs within transversal direction in the auxiliary wall.

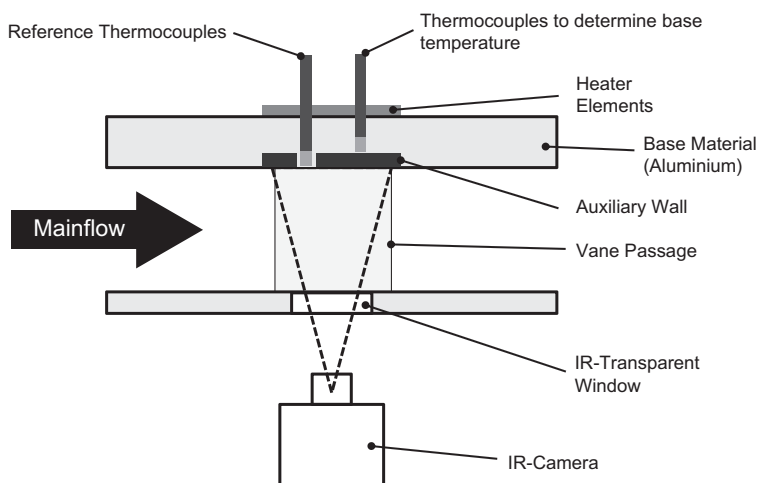


Figure 3. Schematic of the experimental setup.

$$\dot{q}(x, y) = \frac{\lambda_{\text{ETFE}}}{s(x, y)} (T_w(x, y) - T_B(x, y)) \quad (2)$$

The ETFE's thermal conductivity has been measured with a laser-response transition measurement. It has been determined to an average value λ_{ETFE} of 0.195 W/(mK)) and shows only limited dependence to temperature. The absolute value is lower than in the literature for homogeneous ETFE materials. According to the laboratory of Netzsch [15], the manufacturing process and filling materials could be a reason. Since the specific heat is also determined to values below literature, the assumption is fortified. The ETFE is applied through electrostatic powder coating to the aluminium surface. Afterwards, the measurement area is machined to achieve a smooth surface and a layer thickness $s(x, y)$ of between 0.75 and 1 mm. The thickness varies locally and is determined for the whole surface of interest using a laser triangulation measurement system. It has an accuracy of about 5 μm and the surface is scanned on an equally spaced mesh of 0.25 mm, which is a greater resolution than the infrared image. This scan is performed twice: Before applying the ETFE coating and after machining the coating. Hence, for all points on the surface of interest, a local thickness value $s(x, y)$ of the auxiliary wall is known and used in the determination of the surface-normal heat flux $\dot{q}(x, y)$. Finally, the surface is coated with black paint (Nextel Velvet Coating) with an emissivity value ε of 0.97 according to Lohrengel and Todtnhaupt [16].

Infrared thermography is used to determine the surface temperature distribution. An *in situ* calibration of surface temperature values is performed: Reference thermocouples are positioned as close as possible underneath small cylindrical pins the aluminium base material which are not coated with ETFE, but only with black paint. The calibration curve is determined on the basis of Ochs et al. [17]. A schematic of the experimental setup is depicted in Figure 3.

The infrared data is recorded using a FLIR X6540sc camera with an InSb-detector and a spectral response between 2.5 and 5.1 μm . The camera is placed above an uncoated ZnS-glass with a transmissivity τ of 71–73% in the detector range. A frame rate of 10 Hz is used and hence during the 30s-sampling time, 300 thermograms are recorded with 640×512 pixels each. This results in a spatial resolution of at least 0.4 mm on the measurement surface depending on viewing angles. Four overlapping camera positions have been used to cover the area of interest with a minimum of three reference positions in the field of view. In overlapping areas, an arithmetic average is calculated.

As a reference temperature for the heat transfer coefficient (ref. Equation (1)), the local adiabatic wall temperature is deduced according to Gritsch et al. [18]. This requires various subsequent settings of steady state wall temperatures and the corresponding local heat flux values. A linear regression then yields the local wall temperature where no heat flux would occur (Figure 4). The heat transfer coefficient determined in this way is called adiabatic heat transfer coefficient and it will be used in the presentation of all results. Its significance is illustrated by Moffat [19].

Data is recorded for nine different heater settings, leading to base material temperatures between 333 and 373 K. The temperature is controlled by pulse-width-modulation within a band of 0.1 K during data acquisition resulting in a quasi-isothermal distribution in the base material underneath the auxiliary wall.

One of the method's advantage is that it can also be applied to 3D-shaped surfaces. This enables to study engine-realistic combustor-turbine interfaces, with a tapered annulus geometry. The large scale turbine rig (LSTR) at TU Darmstadt offers this possibility

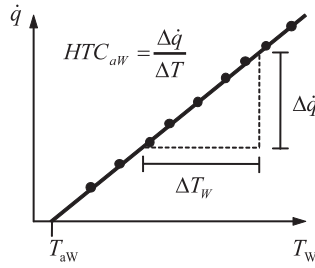


Figure 4. Linear regression to deduce adiabatic heat transfer coefficient HTC^{aW} .

and uses the presented method to study the aerothermal interaction of combustor and turbine with varying inflow conditions, also including a lean combustion aerodynamic (cold) setup. Commissioning results of the simultaneous heat transfer and film cooling effectiveness measurements can be found in Werschnik et al [20]. Numerical Simulations of the planned measurement campaign at the LSTR have been conducted by Schmid et al. [21].

4. Description of the test rig and experiments

The measurements were carried out at the low speed linear cascade test rig at the Institute of Gas Turbines and Aerospace Propulsion, Technische Universität Darmstadt (Figure 5). The rig is operated in suction mode and controlled to a constant Reynolds number of 100,000. The test section is made up of five cascade vanes, whereas the upper endwall between two of the centred vanes is instrumented for heat transfer measurements as described in Section 3. A coolant injection module allows varying both injection rate and geometry upstream of the stator vanes. Two configurations have been studied: A baseline case without coolant injection and a cooled case with a series of 20 holes per stator passage with a diameter D of 4 mm each and a hole spacing of 10 mm in pitch wise direction. The coolant is introduced with a stream wise inclination of 45° . The aerodynamic cooling parameters have been varied as shown in Table 1, the definitions are stated in Equation (3), with the subscript ‘c’ for the cooling air parameters and ‘ ∞ ’ for the main flow data. For the settings in bold, data has been recorded for the whole endwall whereas for the three remaining settings, only the leading edge region has been observed. The thermo-optical access is positioned on the opposing side. The camera is mounted on a rack allowing accurate adjustment of the field of view towards the passage endwall. A more detailed description of the test rig can be

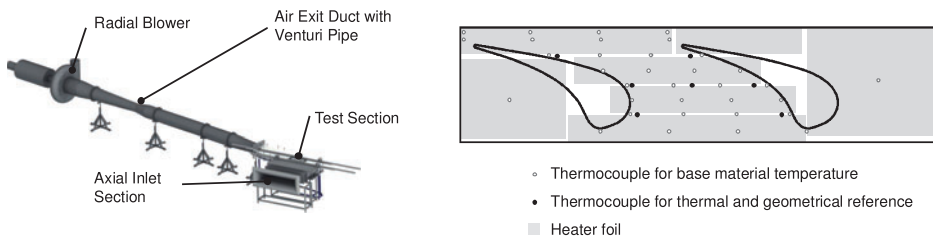


Figure 5. Test rig setup and instrumentation diagram.

Table 1. Aerodynamic film cooling parameters.

Injection rate IR (% \dot{m}_∞)	Blowing ratio M (–)	Density ratio DR (–)	Reynolds number (–)
0	–		
1.6	2.6		
2.4	3.9	1.0	100,000
3.7	6.1		
5.0	8.2		

found in Giller and Schiffer [22], the corresponding numerical work in Schmid and Schiffer [23].

To monitor the base material temperature, an array of 32 thermocouples has been installed, with 7 additional thermocouples representing thermal and geometrical reference values for the infrared image. The positions are shown in Figure 5. Seven heater foils are individually controlled to introduce the heat flux and to keep the base material at a homogenous temperature level within a band of 0.5 K.

$$M = \frac{\rho_c \cdot u_c}{\rho_\infty \cdot u_\infty}, \quad \text{IR} = \frac{\dot{m}_c}{\dot{m}_\infty}, \quad \text{DR} = \frac{\rho_c}{\rho_\infty} \quad (3)$$

The coolant injection module in the present investigation is designed to model hub side coolant injection at the interface of combustor and turbine sections in modern gas turbines. High mass flow rates and blowing rates are realised. In former engine designs, this coolant air flow has mainly been dedicated to reduce the air temperature in the vicinity of the endwall to lower the amount of heat flux into the structure and to seal the combustor turbine interface gap. Current research by Knost and Thole [24] shows, that it can also have a significant cooling effect on parts of the endwall.

5. Endwall heat transfer results

Figure 6 shows the heat transfer coefficient averaged in pitch wise direction – normal to the inflow direction – over the relative axial position in respect to the vane’s axial chord length for both cases. Due to limitations in the optical access, the endwall between two vanes was fully covered up to an x/c_{ax} of 0.9 only.

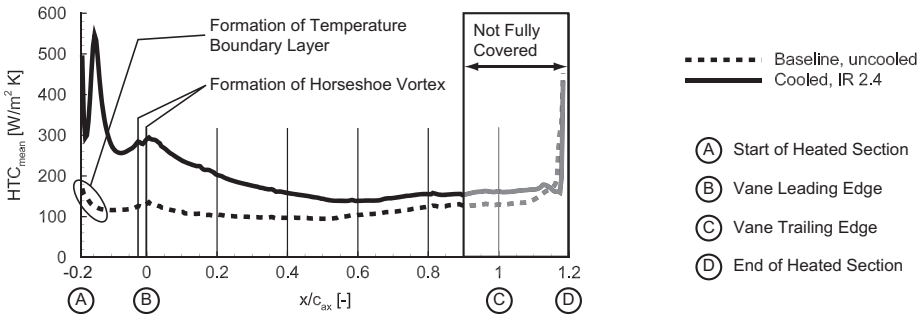


Figure 6. Endwall heat transfer, averaged in pitch wise direction.

For the uncooled case, the heat transfer coefficient yields the typical characteristics for a NGV passage: There is an intermediate peak upstream of the leading edge at x/c_{ax} between -0.03 and -0.01 due to the influence of the vortex system ahead of the stator stage. This is namely the formation of the horseshoe vortex and highlighted in Figure 6. Within the passage, the growing inlet boundary layer causes a decreasing heat transfer coefficient. The newly formed thin boundary layer after the separation line increases the heat transfer coefficient at about mid-passage towards the exit of the vane passage reaching values as high as at the intermediate peak upstream of the leading edge. Since the measurement area is thermally decoupled from the remainder of the test rig, a step change in heat flux occurs at its onset and the thermal boundary layer starts to form at x/c_{ax} of -0.2 , as highlighted.

The coolant injection increases heat transfer throughout the whole passage. However, the dominant effect occurs from the leading edge up to about mid-passage. The characteristic intermediate peak upstream of the leading edge is slightly more pronounced but at a similar position as in the baseline case. The formation of the horseshoe vortex seems to be intensified with increased endwall heat transfer in this area. The heat transfer coefficient then decreases steeper as for the uncooled case towards mid-passage. The change to increasing characteristics begins further downstream in the passage at about x/c_{ax} of 0.65 . Thereafter, the characteristics follow that of the uncooled case with almost the same slope, but with a constant offset of about $50 \text{ W}/(\text{m}^2\text{K})$. Towards the physical end of the measurement area, the heat transfer coefficient heads for infinity in both cases, since the assumption of a non-zero heat flux in planar direction within the auxiliary wall cannot be held up anymore, since the surrounding of the measurement area is not heated but thermally isolated. Thus an in-planar temperature gradient exists at the aft boundary and hence a non-zero, in-planar heat flux occurs. The comparison to the numerical simulation, where the boundary was set to adiabatic, emphasises this aspect.

Figure 7 shows the local distribution of the experimental results. The inflow direction in all contour plots is from bottom to top.

Local maxima for the heat transfer coefficient are identified as follows: A peak is found in the leading edge region of the airfoil where a new boundary layer is formed after the lift-off of the horseshoe vortex system. Near the pressure and suction side corners of the vane the thin boundary layer and high velocities increase heat transfer. The dominating heat transfer peak starts near the shoulder region of the vane suction side, a

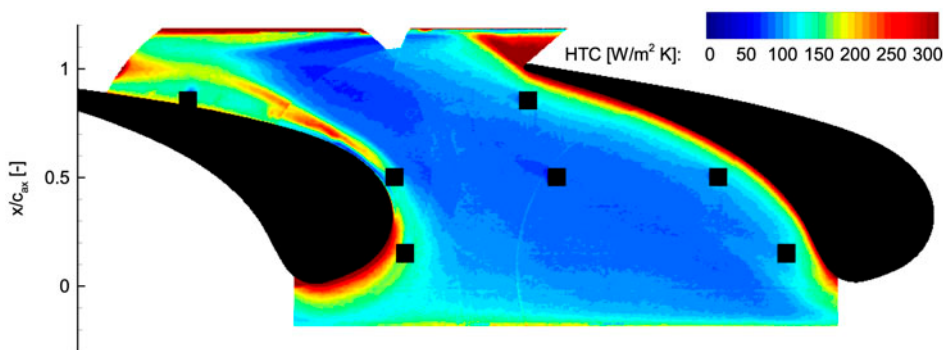


Figure 7. Endwall heat transfer distribution for the baseline case.

reason of the interaction of secondary vortices and high velocities. The last peak is found on the suction side endwall portion downstream of the trailing edge. A possible explanation for this peak could be a flow separation and subsequent reattachment of the flow near the endwall on the suction side. The vane configuration in the test rig seems to be susceptible to separation even for small incidence angles. All regions have been mentioned by previous experiments as regions of high heat transfer excluding the downstream suction side peak. This aspect will be assessed with the numerical simulation. The typical heat transfer distribution seen in the literature with lower heat transfer coefficients upstream of the separation line and high value downstream of it, is not found in the experiments. Whereas in the vicinity of the vanes, the distribution is similar to literature data, the heat transfer coefficient distribution in the centre of the passage is more similar to a flat plate in turbulent inflow.

Local heat transfer is drastically increased downstream of the coolant injection: Figure 8 shows the local distribution for an IR of 2.4. A smaller maximum is found downstream of the injection holes. Maxima with larger extension are located between adjacent holes and further downstream into the passage. The area downstream of two adjacent cooling holes has been magnified to emphasise the location of the maxima. The endwall shows a heat transfer distribution found in the literature [4] for moderate to high blowing rates in coolant injection cases, typical for vortex shedding off a jet-in-crossflow. In general and especially for high blowing rates, the coolant jet acts similar to a cylinder in crossflow, creating air vortex pair downstream of the jet on the endwall with influence on the heat transfer maxima. Hence, for adjacent cooling holes, the maximum is found centric downstream of two holes rather than directly downstream of each hole.

The dominant maximum from the baseline case near the suction side downstream of the vane's shoulder can be found in a similar position for the cooled case, but with less distinct maximum values and an increased spatial distribution. To examine the method's sensitivity to flow field changes, the coolant mass flow and blowing rate of the coolant injection has been varied as mentioned in Table 1. Results are shown for the leading edge region in Figure 9.

It can be seen, that for all four cases, heat transfer peaks are located downstream of the region between adjacent injection holes but not downstream of the holes themselves. The region with higher level heat transfer is increased with the injection rate. For the IR of 5.0, no significant further change occurs compared to the next smaller

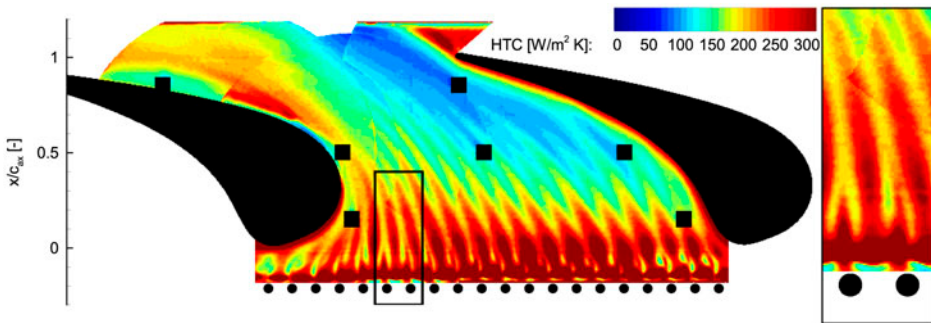


Figure 8. Endwall heat transfer distribution for the cooled case (IR 2.4).

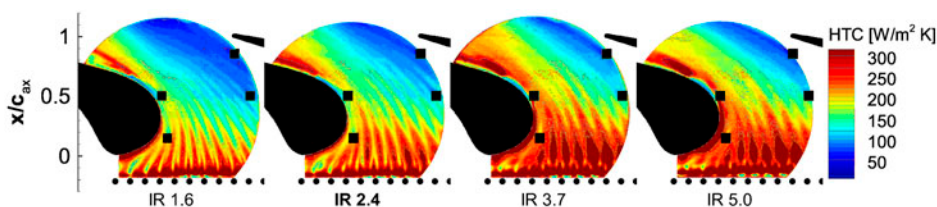


Figure 9. Heat transfer in the leading edge area for varied injection rates.

IR. The location and direction of the increased heat transfer contours does not differ due to the blowing rate. Together with the observations before, this suggests the hypothesis that the coolant does not attach to the wall but protrudes through the boundary layer for all blowing rates.

6. Numerical simulations – setup

One passage of this turbine cascade is investigated numerically for comparison with experimental data. The numerical model includes the main flow path with a single vane of the cascade, as well as the film cooling holes. The topology of the domain is shown in Figure 10. The hub end wall is divided into three sections to enable a specific thermal boundary condition at the walls of the measurement section. An open channel of approximately 17 axial chord lengths is included in the model behind the vane trailing edge in order to prevent the propagation of pitch-wise pressure non-uniformities from the domain outlet towards the measurement section.

The fluid domain is discretised with an unstructured mesh of 16.9 M cells using the commercial software Centaur(TM) 10.6. The grid consists of prismatic layers resolving the boundary layers close to the walls and tetrahedral cells in the inner domain. The boundary layer is resolved with 15 cell layers at the passage end walls and vane and 10 layers in the film cooling holes. Accordingly, the normalised wall distance attains an average value of 1.3 in the passage and 1.2 in the film cooling holes for all simulations conducted. The respective grid is shown in Figure 11.

Steady simulations of the 3D turbulent Navier-Stokes equations are performed using ANSYS 15 CFX. Closure is achieved using the SST-k-omega turbulence model without the modelling of transition.

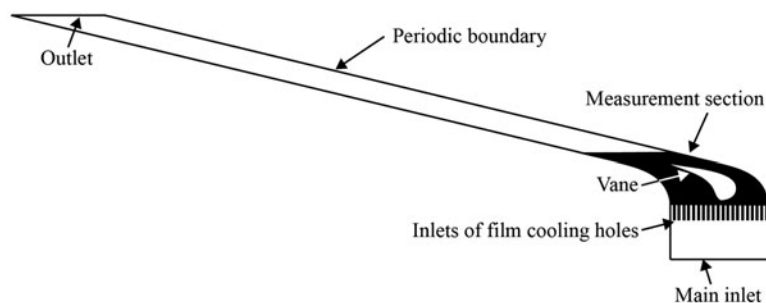


Figure 10. Computational domain.

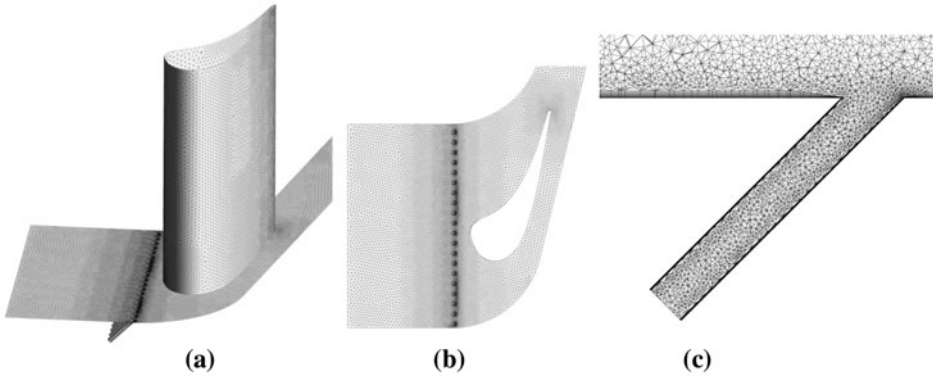


Figure 11. Discretization of vane and channel surface (a, b) and cooling hole (c) in baseline mesh.

In order to determine the mesh sensitivity of the solution, two mesh refinement studies are carried out. Grid spacing and normalised wall distance y^+ are varied with regard to a baseline mesh that is used in the actual simulations. In the grid resolution study two additional meshes which differ only in the size of the tetrahedrons are evaluated. On a fine mesh with 38.4 M cells the grid spacing is reduced by one fourth whereas on a coarse mesh with 9.4 M cells the grid spacing is increased by the same ratio. All meshes inherit the same boundary layer resolution. Figure 12 shows the pitch-wise averaged heat transfer coefficients for these meshes in comparison. It can be seen that from baseline mesh to fine mesh the grid spacing still has an influence on the solution close to the leading edge. The additional computational effort entailed by a further mesh refinement outweighs the benefit of improved accuracy, since the finest mesh already comprises nearly 40 M cells.

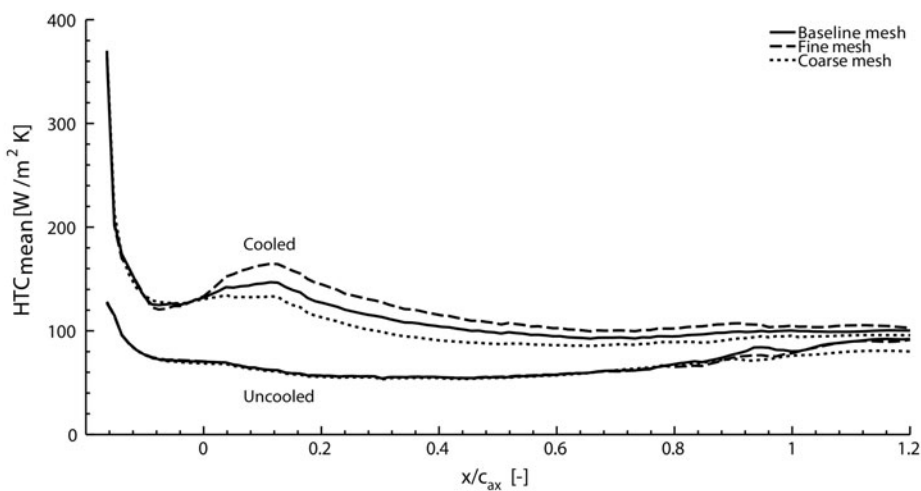


Figure 12. Influence of grid spacing.

Considering that boundary layer behaviour exhibits substantial influence on the heat transfer, the influence of the normalised wall distance is investigated by comparing the baseline mesh with two meshes of halved and doubled wall distance, respectively. Figure 13 shows that the boundary layer resolution of the baseline mesh is sufficient, implying that a solution on this grid is independent of y^+ .

All four injection rates of the experiment from 1.6 to 5.0 are simulated. Boundary conditions are shown in Table 1. The temperature of the measurement section walls is set to a constant value of $T_w = 343.15$ K, while all other walls are modelled adiabatic. As the thermal boundary conditions of main flow and film cooling inlets are both set to 300 K, this temperature is assumed to be the adiabatic wall temperature within the measurement section in order to reduce computational effort. Turbulence intensities are set to 1% at the main and film cooling inlet. For the main inlet, this is in accordance with measurements.

Figure 14 shows that the cascade geometry causes an unequal propagation of outlet pressure through the domain as streamlines on the inner side of the channel are shorter than those on the outer side. The consequence is a pitch wise non-uniformity in inlet pressure and streamline curvature. Thus, the inflow angle α is different for each vane in the experiment. In all simulations the flow angle α is set to 16° which is the inflow condition of the experimentally observed vane at an injection rate of 2.4%.

7. Numerical simulations – results and comparison with experiments

Figure 15 shows the numerically determined local distribution of the heat transfer coefficient for the uncooled case and the cooled case with an injection rate of 2.4%.

A comparison of the HTC values with the experimental data (Figures 7 and 8) within the measurement section, which is indicated by dashed lines, shows a very good qualitative agreement. With regard to the uncooled case, the maxima at the leading edge and downstream of the trailing edge fit very well. Referring to the cooled case, the major characteristics of the heat transfer behaviour shown in the experiments can

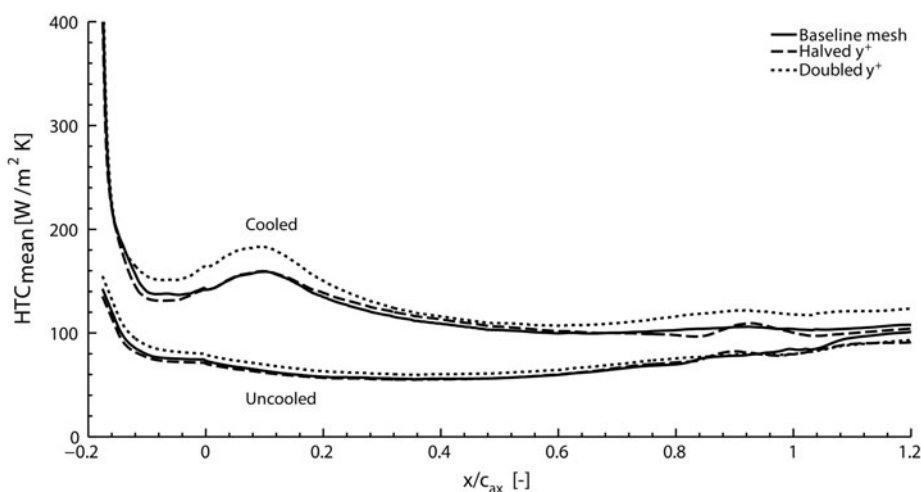


Figure 13. Influence of normalised wall distance.

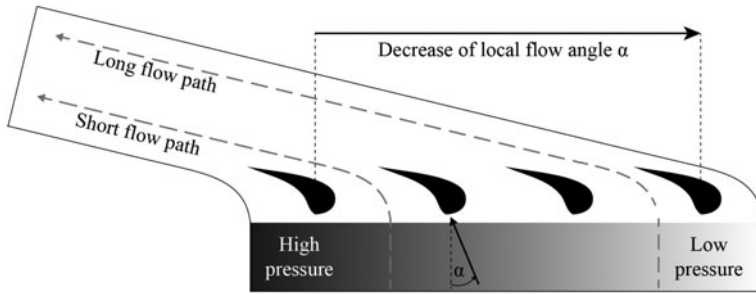


Figure 14. Pitch wise change of the cascade inflow angle.

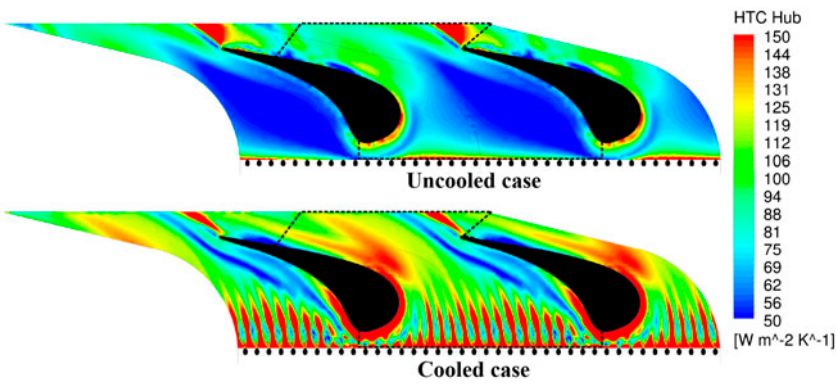


Figure 15. Heat transfer coefficient for baseline case, numerical simulation.

be recognised in the simulation, as well: The heat transfer maxima in between the cooling hole outlets and downstream of the trailing edge as well as the region of high heat transfer in the passage close to the vane's shoulder as observed in the experiments are confirmed by the numerical results. At the leading edge, the numerical simulation over predicts heat transfer. Furthermore, the overall magnitude of heat transfer is considerably lower. It should be noted that the HTC range in the presentation of the numerical results is different from the experiment. This difference may result from an under prediction of turbulent kinetic energy from the use of the $k-\omega$ -turbulence model. This assumption is based on a numerical simulation of the same set-up using the $k-\varepsilon$ -model which results in a higher prediction of turbulent kinetic energy and a much better agreement of the HTC magnitude. As the main flow features are qualitatively best predicted by the SST $k-\omega$ -turbulence model, it is used in the presented simulations.

Results of the numerical simulations at four injection rates are shown in Figure 16 with the experimentally observed section marked by a dashed line. It can be seen in Table 2 that a constant inflow angle is used for all simulations. For an increase in injection rates, a turning of the HTC streaks towards the axial direction is observable which may be explained by the higher momentum of the jets at high injection rates.

The simulations confirm the observations of the experiments that the overall level of HTC increases and a region of high HTC occurs at the leading edge with increasing injection rates. As observed in the experiments, a peak of HTC is found on the suction

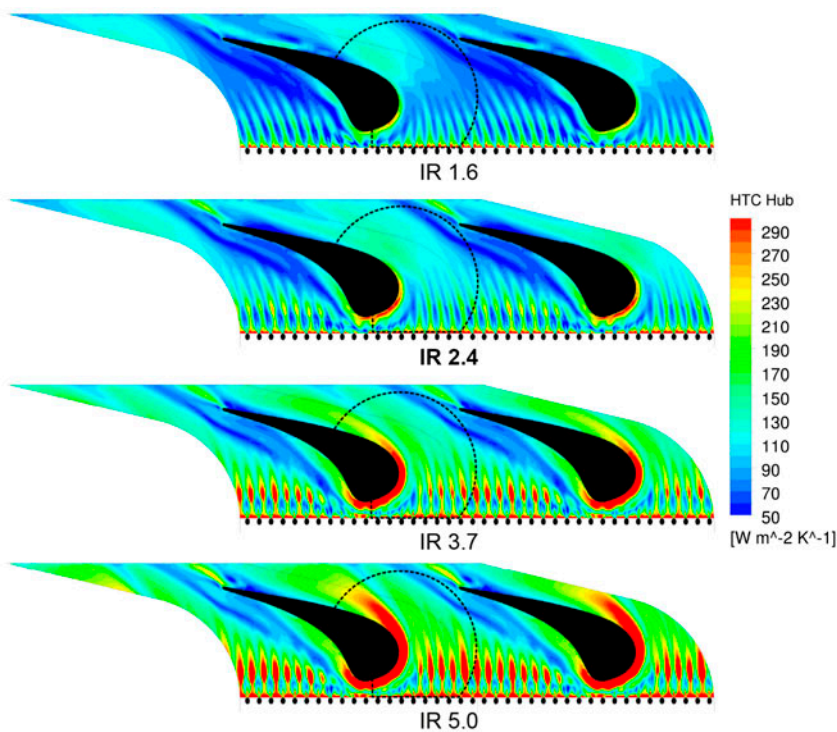


Figure 16. Heat transfer coefficient for varied injection rates, numerical simulation.

Table 2. Boundary conditions – numerical simulation.

Main inlet (const.)	Film cooling inlets (const.)	Main outlet (avg.)
$\dot{m}_{\infty} = 0.425 \text{ kg/s}$	$\dot{m}_c = 1.6 - 5.0\% \text{ of } \dot{m}_{\infty}$	$p_{\text{out}} = 97600 \text{ Pa (abs)}$
$T_{\infty} = 300 \text{ K}$	$Tu_c = 1\%$	Measurement section walls
$Tu_{\infty} = 1\%$	$T_c = 300 \text{ K}$	$T_w = 343.15 \text{ K}$
$\alpha = 16^{\circ} \text{ (w.r.t. axial dir.)}$	Normal inflow direction	

side end wall portion downstream of the trailing edge. It has been mentioned earlier that flow separation may be an explanation for this behaviour which can be affirmed by the CFD results. Figure 17 shows streamlines along the suction side surface of the blade (depicted by black lines) as well as streamlines on an additional plane in the passage (white lines). It can be seen that there is indeed flow separation on the end wall close to the suction surface which leads to a minimum region of heat transfer. Further downstream a vortex structure is visible which looks very similar to the corner vortex [4] shown in Figure 1. This vortex contributes to a re-attachment of the flow implicating a substantial rise in HTC.

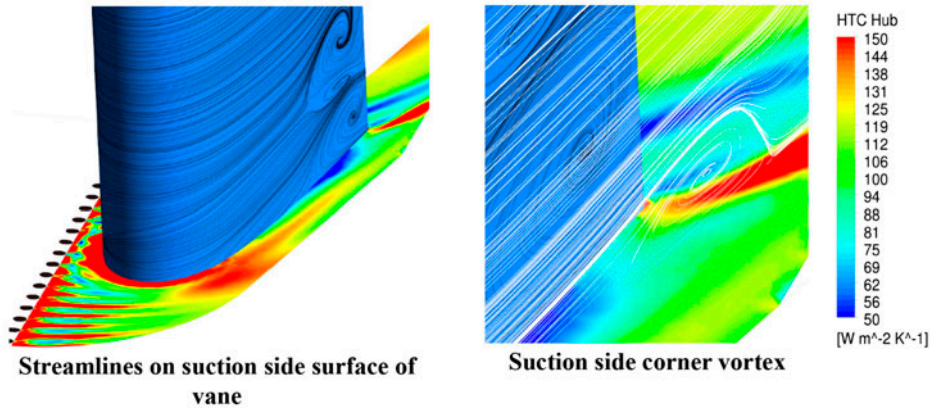


Figure 17. Trailing edge secondary flow.

8. Conclusion and outlook

A method has been developed to study local heat transfer coefficients on turbine stator endwalls. The use of a powder coated and machined auxiliary wall enables the use of this measurement technique also on 3D-shaped surfaces. To validate the technique, measurements have been conducted at a linear cascade rig. Heat transfer has been studied for an uncooled baseline case as well as for a second case with hub side coolant injection upstream of the leading edge.

Heat transfer peaks are determined upstream of the leading edge, near the vane's pressure side and suction side corners, downstream of the trailing edge and a dominant maximum near the suction side shoulder section of the endwall. The maximum downstream of the trailing edge is thought to result from a flow separation. All other maxima are usually found in the literature as well.

Coolant injection increases heat transfer on the endwall. The increase is greater near the injection holes and for higher injection rates. The peaks in the leading edge region and near the suction side shoulder of the vane are also found for the cooled case with increased spatial distribution.

A numerical simulation of the experiment is used to relate the results to the flow field phenomena in the test rig. The results for the uncooled case are comparable to the experimental results, however the heat transfer level is under predicted in the numerical simulation. The maximum at the downstream suction side of the endwall, which is usually not found in the literature, can be explained by the numerical simulation.

The results show the current state of the data analysis tools. In the future it is planned to further optimise the geometrical and thermal calibration processes. Further data on the aerodynamic flow field will accompany the thermal measurements to acquire a deeper insight into the flow features which influence endwall heat transfer.

The method itself will be used for future experiments in a rotating turbine rig and with more realistic geometries of the combustor-turbine interface in aeroengines with variable inflow conditions and again compared to numerical simulations.

Nomenclature

α	Inflow angle
D	Cooling hole diameter
DR	Density ratio, $DR = \rho_c / \rho_\infty$
ε	Emissivity
ETFE	Ethylene-Tetrafluoroethylene
HTC	Heat transfer coefficient, $HTC(x, y) = \frac{\dot{q}(x, y)}{(T_w(x, y) - T_{ref})}$
IR	Injection rate, $IR = \dot{m}_c / \dot{m}_\infty$
λ	Thermal conductivity
LSTR	Large scale turbine rig
M	Blowing ratio, $M = \frac{\rho_c \cdot u_c}{\rho_\infty \cdot u_\infty}$
NGV	Nozzle guide vane
η	Film cooling effectiveness, $\eta = \frac{T_\infty - T_w}{T_\infty - T_c} \approx \frac{c_\infty - c_w}{c - c_c}$
\dot{q}	Local heat flux, $q(\dot{x}, y) = -\frac{\lambda}{s(x, y)} \cdot (T_w(x, y) - T_B(x, y))$
RIDN	Rear inner discharge nozzle
s	Layer thickness
τ	Transmissivity
T	Temperature
Tu	Turbulence level
x/c_{ax}	Axial position relative to axial vane chord length
y^+	Normalised wall distance
<i>Subscripts</i>	
ax	Axial chord
B	Base material
c	Coolant flow property
ref	Reference value
w	Wall
∞	Main flow property

Acknowledgments

The contribution of Marcel Adam and Lars Ohde is gratefully acknowledged.

Disclosure statement

No potential conflict of interest was reported by the authors.

Funding

The work reported was partly funded within the framework of the “AG Turbo” by the Federal Republic of Germany, Ministry for Economic Affairs and Energy, according to a decision of the German Bundestag [grant number FKZ: 03ET2013K] as well as by Rolls-Royce Deutschland GmbH; ALSTOM Power.

References

- [1] Friedrichs S. Endwall film cooling in axial flow turbines [dissertation]. Cambridge: Cambridge University; 1997.
- [2] Han J, Datta S, Ekkad S. Gas turbine heat transfer and cooling technology. 2nd ed. Boca Raton, FL: CRC Press/Taylor & Francis; 2013. xvii, 869. ISBN: 978-1-4398-5568-3.

- [3] Goldstein RJ, Spores RA. Turbulent transport on the endwall in the region between adjacent turbine blades. *J. Heat Transfer*. 1988;110(4a):862–869.
- [4] Dückershoff R. Filmkühlung in Gebieten mit verzögerter Hauptströmung und in Bereichen lokaler Strömungsablösung [dissertation, Film Cooling in areas of decelerated main flow and in areas of local flow separation]. Aachen XIV: Shaker Verlag; 2004, 144 S.
- [5] Friedrichs S. Aerodynamic aspects of endwall film-cooling. *J. Turbomach.* 1997;119(4):786–793.
- [6] Lazik W, Doerr T, Bake S. Low NO_x combustor development for the engine3E core engine demonstrator. ISABE-Paper 2007-1190; 2007.
- [7] Han S, Goldstein RJ. Heat transfer study in a linear turbine cascade using a thermal boundary layer measurement technique. *J. Heat Transfer*. 2007;129(10):1384–1394.
- [8] Blair MF. An experimental study of heat transfer and film cooling on large-scale turbine endwalls. *J. Heat Transfer*. 1974;96:524–529.
- [9] Graziani RA, Blair MF, Taylor JR, Mayle RE. An experimental study of endwall and airfoil surface heat transfer in a large scale turbine blade cascade. *J. Eng. Power*. 1980;102(2):257–267.
- [10] Giel PW, Thurman DR, van Fossen GJ, Hippensteele SA, Boyle RJ. Endwall heat transfer measurements in a transonic turbine cascade. NASA Technical Memorandum. 1996; 107387-1–107387-15.
- [11] Giel PW, van Fossen GJ, Boyle RJ, Thurman DR, Civinskas KC. Blade heat transfer measurements and predictions in a transonic turbine cascade. NASA Technical Memorandum. 1999;1996:2009296:1–15.
- [12] Kaiser E. Zur Wärmestrommessung an Oberflächen unter besonderer Berücksichtigung von Hilfs wand-Wärmestromaufnehmern [dissertation, On the measurement of heat flux on surfaces with special respect to auxiliary wall heat flux gauges]. Dresden: Eigenverlag; 1982.
- [13] Martini P, Schulz A, Bauer H. Film cooling effectiveness and heat transfer on the trailing edge cutback of gas turbine airfoils with various internal cooling designs. *J. Turbomach.* 2006;128:196–205.
- [14] Laveau B, Abhari RS, Crawford ME, Lutum E. High resolution heat transfer measurements on the stator endwall of an axial turbine. *J. Turbomach.* 2014;137(4):041005–041014.
- [15] Netzsch Gerätebau GmbH. Thermophysikalische Eigenschaften von 1 ETFE Materialprobe [Thermophysical properties of a ETFE sample]. Selb: Netzsch Gerätebau GmbH; 2013 (3257-P-13).
- [16] Lohrengel J, Todtnhaupt R. Wärmeleitfähigkeit, Gesamtmissionsgrad und spektrale Emissionsgrade der Beschichtung Nextel-Velvet-Coating 811 (RAL 900 15 tiefschwarz matt). [report 106 of the federal technical board of germany, Thermal conductivity, total emissivity and spectral emissivity of the coating Nextel-Velvet-Coating 811 (RAL 900 15 dark black, opal)]. PTB-Mitteilungen. Vol. 106, Braunschweig; 1996.
- [17] Ochs M, Horbach T, Schulz A, Koch R, Bauer H. A novel calibration method for an infrared thermography system applied to heat transfer experiments. *Meas. Sci. Technol.* 2009;20(7):075103-1–075103-9.
- [18] Gritsch M, Baldauf S, Martiny M, Schulz A, Wittig S. The superposition approach to local heat transfer coefficients in high density ratio film cooling flows. In: ASME 1999 International Gas Turbine and Aeroengine Congress and Exhibition, Indianapolis; 1999. p. V003T01A048.
- [19] Moffat RJ. $h_{\text{sub adiabatic}}$ and $u_{\text{sub max}}^*$. *J. Electron. Packag.* 2004;126:501–509.
- [20] Werschnik H, Krichbaum A, Schiffer H, Lehmann K. The influence of combustor swirl on turbine stator endwall heat transfer and film cooling effectiveness in a 1.5-stage axial turbine. ISABE-Paper 2015-20184; 2015.
- [21] Schmid G, Krichbaum A, Werschnik H, Schiffer H. The impact of realistic inlet swirl in a 1 ½ stage axial turbine. In: ASME Turbo Expo 2014: Turbine Technical Conference and Exposition, Düsseldorf; 2014. p. V02CT38A045.
- [22] Giller L, Schiffer H. Interactions between the combustor swirl and the high pressure stator of a turbine. In: ASME Turbo Expo 2012: Turbine Technical Conference and Exposition, Copenhagen; 2012. p. 1401.
- [23] Schmid G, Schiffer H. Numerical investigation of inlet swirl in a turbine cascade. In: ASME Turbo Expo 2012: Turbine Technical Conference and Exposition, Copenhagen; 2012. p. 543.
- [24] Knost DG, Thole KA. Adiabatic effectiveness measurements of endwall film-cooling for a first-stage vane. *J. Turbomach.* 2005;127:297–305.